

Probing Hidden Mott Gap and Incommensurate Charge Modulation on the Polar Surfaces of PdCrO₂

Chenhaoping Wen,^{1,*} Tian Qin,^{1,*} Xuefeng Zhang,^{1,*} Mingxin Zhang,^{1,*} Weixiong Hu,¹ Shiwei Shen,¹ Zhongzheng Yang,¹ Yanpeng Qi,^{1,2,3,†} Gang Li,^{1,2,‡} and Shichao Yan^{1,2,§}

¹*School of Physical Science and Technology, ShanghaiTech University, Shanghai 201210, China*

²*ShanghaiTech Laboratory for Topological Physics, ShanghaiTech University, Shanghai 201210, China*

³*Shanghai Key Laboratory of High-resolution Electron Microscopy, ShanghaiTech University, Shanghai 201210, China*



(Received 30 January 2023; revised 7 June 2023; accepted 23 August 2023; published 15 September 2023)

Here we report a combined study of low-temperature scanning tunneling microscopy and dynamical mean-field theory on PdCrO₂, a delafossite metal with an antiferromagnetic order below ~ 37.5 K. First, on the CrO₂-terminated polar surface we detect a gaplike feature both below and above the Néel temperature. The dynamical mean-field theory calculations indicate that this gap is opened due to the strong correlations of Cr-3*d* electrons, suggesting the hidden Mott nature of the gap. Then, we observe two kinds of Pd-terminated polar surfaces. One is a well-ordered Pd surface with the Fermi-surface-nesting-induced incommensurate charge modulation, while the other one is a reconstructed Pd surface with the individual nanoscale nonperiodic domain structures. On the well-ordered Pd surface, the interference between the incommensurate charge modulation and the atomic lattice forms the periodic moiré pattern. Our results provide important microscopic information for fully understanding the correlated electronic properties of this class of materials.

DOI: [10.1103/PhysRevLett.131.116501](https://doi.org/10.1103/PhysRevLett.131.116501)

Correlated electronic phases often emerge accompanied by the antiferromagnetic (AFM) order, such as the unconventional superconductivity in cuprates and iron-based superconductors [1–3]. Fully understanding these correlated electronic phases is challenging because of the complicated interplay among different electronic orders, such as antiferromagnetism, nematicity, and superconductivity [1–3]. Exploring the interaction between the conduction electrons and the localized magnetic moments in a simpler material would be helpful to gain a deeper understanding of the correlated electronic systems. In this respect, the delafossite compound PdCrO₂, a natural heterostructured material with individual layers containing itinerant electrons and localized spins, meets this condition [4–9].

Sharing the same crystal structure as the typical delafossite materials, PdCrO₂ consists of the alternative stacking of the triangular Pd layer and CrO₂ layer [8,10–12], in which the Cr and Pd atoms offer 3*d* and 4*d* electrons with distinct responses to charge and spin fluctuations. PdCrO₂ shows metallic conductivity due to the Pd 4*d*⁹ electrons, and the localized spins of Cr³⁺ ($S = 3/2$) lead to the onset of an AFM order with the Néel temperature (T_N) of ~ 37.5 K [13]. According to the neutron scattering measurements, the spin order in PdCrO₂ has a 120° AFM spin structure with $\sqrt{3} \times \sqrt{3}$ periodicity [14–16], but the unconventional anomalous Hall effect found in PdCrO₂ suggests that it may have a chiral spin structure at low temperature [17].

Both the quantum oscillations and angle-resolved photoemission spectroscopy (ARPES) measurements show that the Fermi surface of PdCrO₂ is a single hexagon above T_N , which mainly originates from the Pd electrons [5,18–20]. This hexagonal Fermi surface is backfolded into the antiferromagnetic Brillouin zone below T_N [18–20]. More recently, the combined density functional theory with dynamical mean-field theory (DFT + DMFT) calculations suggest that the Cr layer shows a Mott gap behavior that is driven by the Cr 3*d* local moments [4,21,22]. So far, the microscopic electronic information on the Pd and the CrO₂ layers, which is essential for fully understanding the electronic behaviors of this material, is still lacking.

Here we use low-temperature scanning tunneling microscopy (STM) and DFT + DMFT to systematically study PdCrO₂. Our STM data provide complete information for both the CrO₂- and Pd-terminated polar surfaces. On the CrO₂-terminated surface, we observe a gaplike feature both below and above T_N , which is opened for the Cr 3*d* electrons driven by electronic correlations. On the Pd-terminated surface, we observe a Fermi-surface-nesting-induced incommensurate charge modulation, which is consistent with our DMFT-based random phase approximation (RPA) calculations. In addition, we also observe the influence of Pd vacancies to the incommensurate charge modulation. Our results provide detailed microscopic information for the polar surfaces of PdCrO₂.

Single crystals of PdCrO_2 were grown with a similar procedure as reported in Refs. [10,23]. STM experiments were performed with a Unisoku 1200 low-temperature STM. PdCrO_2 single crystals were cleaved at 77 K with the pressure under 2×10^{-10} Torr, and then were immediately transferred into the STM head for measurements at 4.3 K. The K atoms were thermally evaporated from K source (SAES, Alkali metal dispenser) onto PdCrO_2 at 4.3 K. Scanning tunneling spectroscopy (STS) measurements were done by using a standard lock-in technique. For the theoretical understanding, we constructed a model Hamiltonian consisting of Pd $4d$ and Cr $3d$ orbitals by using the WANNIER90 package [24] and performed DMFT calculations [25,26] with our homemade code *PACS*. Our DMFT calculations were performed in the paramagnetic phase with a temperature $T \sim 290$ K. Continuous-time quantum Monte Carlo method [27] was used as the impurity solver.

Because of the quasi-two-dimensional crystal structure of PdCrO_2 , there is a 50:50 chance of finding the Pd or the CrO_2 surface after cleaving [Figs. 1(a) and 1(b)]. Figures 1(c) and 1(e) are the large-area STM topographies

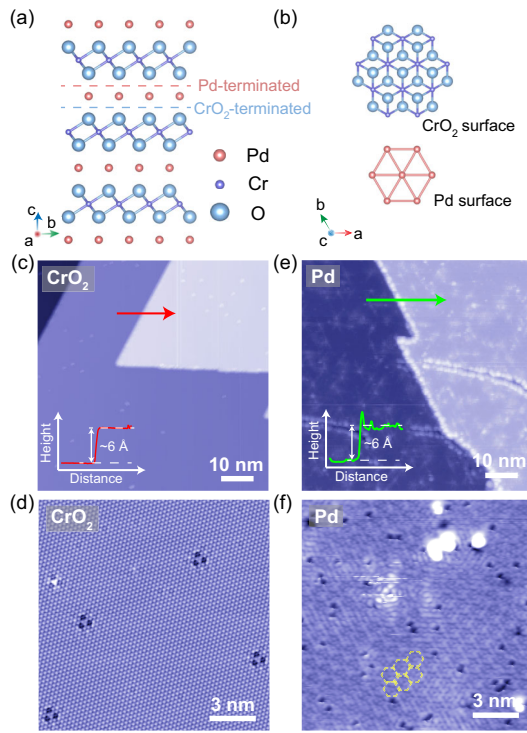


FIG. 1. (a) Crystal structure of PdCrO_2 from the side view. (b) Crystal structures of the CrO_2 (top) and the Pd (bottom) surfaces from the top-down view. (c) STM topography showing the atomic steps on the CrO_2 surface. The inset is the line profile along the red arrow. ($V_s = -500$ mV, $I = 10$ pA). (d) High-resolution STM topography on the CrO_2 surface. ($V_s = -500$ mV, $I = 50$ pA). (e),(f) The same as those in (c) and (d) but measured on the Pd surface. The dashed yellow hexagons in (f) indicate the hexagonal superstructures. (e) $V_s = 200$ mV, $I = 20$ pA and (f) $V_s = 50$ mV, $I = 20$ pA.

taken on the CrO_2 - and the Pd-terminated surfaces, respectively (see Figs. S1 and S2 [28]). As shown in the line profile across the atomic steps [insets of Figs. 1(c) and 1(e)], both the two surfaces show clean and sharp atomic steps with a similar step height (~ 6 Å), indicating that both steps contain one complete CrO_2 -Pd or Pd- CrO_2 unit along the c direction. As shown in Fig. 1(d), on the CrO_2 surface, we observe the triangular atomic lattice with a lattice constant of ~ 2.9 Å and two types of atomic defects. On the Pd surface, except for the atomic structure, we also find the hexagonal patterns with a larger real-space period than the atomic lattice [as indicated by the yellow dashed hexagons in Fig. 1(f)], making the Pd surface distinct from the CrO_2 surface.

We next investigate the two surface terminations separately. First, we perform STS measurements on the CrO_2 surface to reveal its electronic structure [Fig. 2(b)]. At 4.3 K, the dI/dV spectra taken on a defect-free region of the CrO_2 surface show a gaplike feature at the Fermi level (E_F). This gaplike feature is homogeneous on the CrO_2 surface, and its size can barely be affected by the atomic impurities on the surface (see Fig. S3 [28]). Below and beyond the gap, we observe two electronic peaks locating at -0.43 and 0.7 V. For some atomic defects, the spectral intensity is enhanced from -0.5 V to -1 V. The dI/dV spectrum is also consistent with the previous ARPES results on PdCrO_2 (see Fig. S4 [28]). Interestingly, we are still able to detect the finite density of states (DOS) within the energy gap [inset of Fig. 2(b)], which could be contributed by the electrons from the underneath Pd layer.

To understand the nature of the gaplike feature on the CrO_2 surface, we calculate the correlated electronic structure of PdCrO_2 by using DMFT (see Supplemental Material for more details [28]). Figure 2(c) shows the spectral function $A(\mathbf{k}, \omega)$ of PdCrO_2 in the $k_z = 0$ plane. Along the Γ - K and Γ - M direction, a single band with large Fermi velocity crosses E_F , which mainly consists of the Pd $4d$ electrons. Compared to the DFT [22], the electronic states of the Cr $3d$ electrons, however, have been pushed away from E_F by the on-site Hubbard interaction. The lower and the upper Hubbard band stay below -0.4 eV and above 0.1 eV, respectively. The Mott gap is of the size of ~ 0.5 eV, which is highly consistent with our STS measurements. Our paramagnetic DMFT results indicate that it is the electronic correlations and local fluctuations of the Cr $3d$ electrons rather than the long-range orders that open the gap, which is a compelling evidence for the Mott physics that equally applies to the temperatures below and above T_N .

To further confirm this conclusion, we investigate the evolution of the gap size as a function of temperature from below to above the T_N . Figure 2(d) shows the temperature dependence of the dI/dV spectrum taken on the CrO_2 surface. The insulating gap can still be seen even when the temperature is increased up to ~ 78 K. The electronic gap is

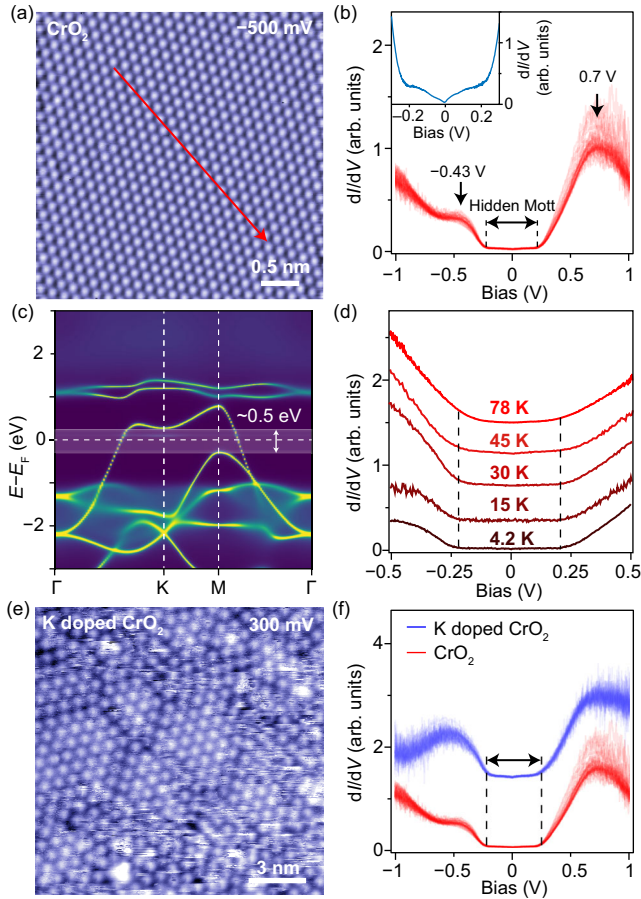


FIG. 2. (a) STM topography taken on the defect-free region of the CrO_2 surface. ($V_s = -500$ mV, $I = 20$ pA). (b) dI/dV spectra taken along the red arrow in (a) (setup condition: $V_s = -1$ V, $I = 1$ nA). Inset: averaged smaller-range dI/dV spectrum taken along the same line (setup condition: $V_s = -250$ mV, $I = 500$ pA). (c) Calculated spectral function $A(\mathbf{k}, \omega)$ along the high-symmetry lines in the reciprocal space. (d) Temperature-dependent dI/dV spectra measured on the CrO_2 surface (setup condition: $V_s = 1$ V, $I = 1$ nA). (e) STM topography taken on the K-doped CrO_2 surface ($V_s = 300$ mV, $I = 5$ pA). (f) Comparison of the dI/dV spectra taken on the pristine (red) and K-doped (blue) CrO_2 surfaces (setup condition: $V_s = 1$ V, $I = 1$ nA).

preserved across the AFM phase transition of PdCrO_2 (~ 37.5 K), which agrees with our DMFT calculations that the Mott gap is opened even when the system is in the paramagnetic state. We also note that the Mott gap on the CrO_2 surface can barely be tuned by the surface K doping, as shown in Figs. 2(e) and 2(f). We dope K atoms with the amount of 0.15 K atoms per unit cell to the CrO_2 surface (see Fig. S5 [28]). Upon doping K onto the surface, we only observe a slight downshift of the peaks of the occupied states, and we find no in-gap states appear in the Mott gap. This might be because the CrO_2 surface is a negatively charged polar surface, and the K atoms cannot dope electrons into it.

Having characterized the CrO_2 surface, we turn to the Pd-terminated surface. Different from the atomic lattice on the CrO_2 surface, the Pd surface has a regular lattice with ~ 4.0 Å periodicity, which is ~ 1.38 times of the lattice constant on the CrO_2 surface (see Fig. S6 [28]). The STM topographies taken on the Pd surface of PdCrO_2 change dramatically as changing the STM bias voltages (see Fig. S7 [28]). Apart from the regular lattice, the striplike patterns appear near the impurities in the STM topography taken with $+200$ mV bias voltage [Fig. 3(a)]. The striplike patterns can usually spread to a distance up to ~ 10 nm. In the STM topography taken with the negative bias voltages [Fig. 3(b)], a superstructure with larger periodicity (~ 9.7 Å) appears.

To quantify the periodicities of the regular lattice and the superstructure on the Pd surface, we perform Fourier transform (FT) to the STM topographies taken on the Pd surface (see Fig. S8 [28]). Figures 3(c) and 3(d) show the FT images of the topographies in Figs. 3(a) and 3(b), respectively. We find that there are three sets of wave vectors marked by the orange (Q_0), blue (Q_1), and green (Q_{Bragg}) circles. The Q_{Bragg} corresponds to the atomic lattice on the Pd surface which has a period of ~ 2.9 Å. The Q_0 wave vector is along the Q_{Bragg} direction while the Q_1 wave vector has an angle of 30° with the Q_{Bragg} wave vector. The lengths of the Q_1 and Q_0 wave vectors are independent of bias voltages as shown in the line profiles in the FT images along the Q_1 and Q_{Bragg} directions (see Fig. S9 [28]). This indicates that the Q_1 is not related with quasiparticle interference. The ratio between the Q_1 and Q_{Bragg} wave vectors is $\sim 0.74 \pm 0.02$, and the ratio between the Q_0 and Q_{Bragg} wave vectors is $\sim 0.30 \pm 0.02$ [Fig. 3(e)]. This indicates that the Q_1 wave vector corresponds to the regular lattice of ~ 4.0 Å and the Q_0 wave vector corresponds to the large periodicity of ~ 9.7 Å.

To explore the origin of the Q_1 wave vector on the Pd surface, we calculate the correlated Fermi surface of PdCrO_2 . According to the DMFT calculations, the Fermi surface is mainly contributed by the Pd layer [Fig. 3(g)], and it is almost a perfect hexagon [5]. The parallel segments on the hexagonal Fermi surface can provide a strong nesting effect, as indicated by the red arrows of q_1 , q_2 , and q_3 . We also calculate the charge susceptibility which is shown in Fig. 3(h) by using the RPA method based on the DMFT correlated electronic structure. We find that the charge susceptibility maximum appears along the Γ -M direction, which has a ratio of ~ 0.74 compared to the reciprocal vector. This ratio matches the measured ratio between Q_1 and Q_{Bragg} , indicating that Q_1 is likely to be induced by the Fermi surface nesting. The nesting-induced charge instability in PdCrO_2 starkly contrasts with the conventional ones, as it emerges from a two-step process that is peculiar to this system. The CrO_2 and Pd layers are geometrically separated and electronically loosely coupled, such that the joint Fermi

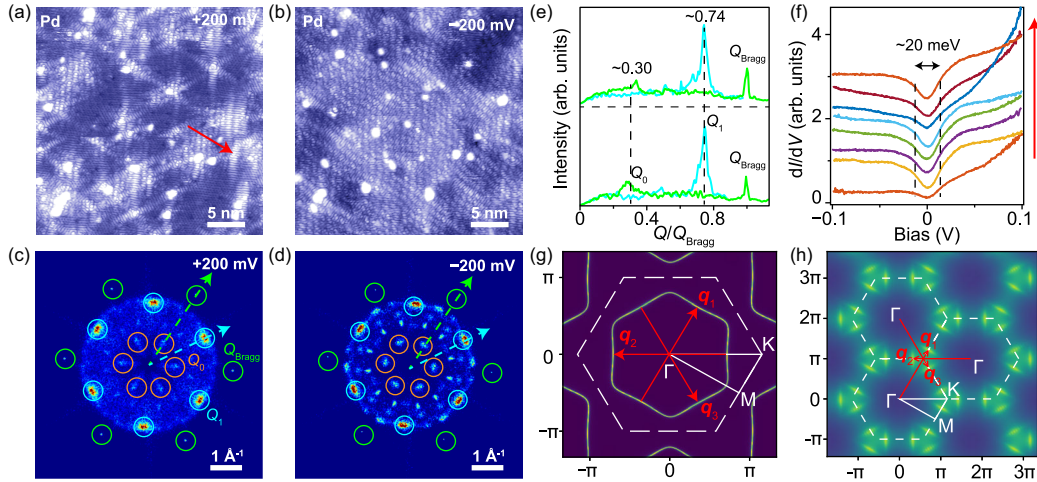


FIG. 3. (a),(b) STM topographies taken on the Pd surface with (a) 200 mV and (b) -200 mV bias voltages, respectively. (c),(d) FT images of the STM topographies in (a) and (b). The green, blue, and orange circles correspond to the Q_{Bragg} , Q_1 , and Q_0 wave vectors, respectively. (e) Line profiles of the FT images in (c) and (d) along the Q_{Bragg} and Q_1 wave vectors. (f) The dI/dV spectra taken along the red arrow in (a) (setup condition: $V_s = 100$ mV, $I = 300$ pA). (g) Calculated Fermi surface of PdCrO₂ in the Brillion zone along the $k_z = 0$ plane. (h) Calculated charge susceptibility by using DMFT-based RPA method. The red arrows in (g) and (h) indicate the nesting vectors.

surface is first renormalized by the electronic correlation of Cr and forms a nesting hexagon that triggers the charge instability in the second step. The emergent Q_1 wave vector in the FT images of the topographies offers a piece of new evidence for the novel correlation effect in this $3d$ - $4d$ hybrid compound. The dI/dV spectra on the Pd surface exhibit metallic behavior between -0.5 and 0.5 V, and have a ~ 20 meV diplike feature near E_F , which could be the gap related to this charge modulation [Fig. 3(f)]. Since the previous ARPES measurements indicate that the size of the bulk Fermi surface of PdCrO₂ has little temperature dependence [5,18], it should remain the same nesting structure as the temperature varies.

Because the charge modulation on the Pd surface is incommensurate with the atomic lattice, it can create an interference pattern with the atomic lattice and form the moiré pattern with larger periodicity. The Q_0 wave vector shown in Figs. 3(c) and 3(d) corresponds to the moiré superlattice of the charge modulation and the atomic lattice (see Fig. S10 [28]). Such Q_0 and Q_1 wave vectors have also been recently reported on the Pd-terminated surface of PdCoO₂, where the Q_1 wave vector is related to the charge modulation pattern, and the Q_0 wave vector is due to the interference between the Q_1 and Q_{Bragg} related lattices [29]. This indicates that this charge instability induced by Fermi surface nesting and the related moiré pattern are common features for the Pd surface of the delafossite metals with hexagonal Fermi surface. These features should be considered for fully understanding the electronic structure on the Pd surface of delafossite metals [30].

Interestingly, except for the well-ordered Pd surface, we also observe another Pd surface with reconstructed patterns. Figure 4(a) shows an atomic step between the reconstructed

Pd surface and the CrO₂ surface, and the step height is ~ 4 Å (see Fig. S11 [28]). We can clearly see that there are nanoscale domains consisting of the semioordered Pd atoms

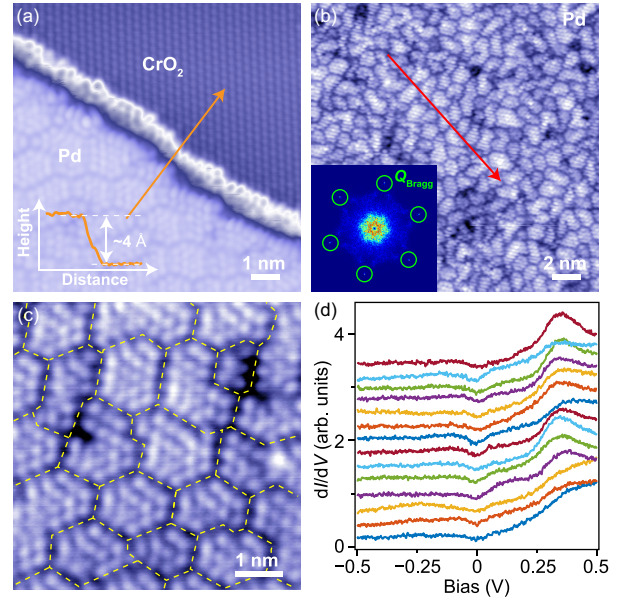


FIG. 4. (a) STM topography measured near the atomic step between the reconstructed Pd surface and the CrO₂ surface. The inset is the line profile along the orange arrow ($V_s = -500$ mV, $I = 20$ pA). (b) STM topography taken on the reconstructed Pd surface ($V_s = -500$ mV, $I = 20$ pA). The inset shows its FT image. (c) Enlarged STM topography on the reconstructed Pd surface. The yellow dashed lines mark the positions of the domain boundaries ($V_s = -500$ mV, $I = 20$ pA). (d) dI/dV spectra measured along the red arrow in (b) (setup condition: $V_s = 500$ mV, $I = 150$ pA).

[Fig. 4(b)]. These domains have different sizes and shapes, and are separated by dark boundaries [as marked by the yellow dashed lines in Fig. 4(c)]. The regular size of the domain ranges from 1 to 2 nm. The spatially resolved dI/dV spectra indicate that the DOS is almost unchanged on the domain boundaries [Fig. 4(d)]. The boundaries between the domains could be induced by the missing Pd atoms during the cleaving process, which may indicate that Pd vacancies can suppress the incommensurate charge modulation on the Pd surface of PdCrO₂.

In summary, we report a systematic study of the polar surfaces of PdCrO₂. On the CrO₂-terminated surface, we detect a hidden Mott gap both below and above the Néel temperature. The DMFT calculations indicate that this hidden Mott gap is opened due to the electronic correlations and fluctuations of the Cr 3d electron local moments. On the well-ordered Pd surface, we detect an incommensurate charge modulation originating from the Fermi surface nesting, which is supported by our renormalized RPA calculations. We also find that Pd vacancies may suppress the incommensurate charge modulation on the Pd surface. Our results provide important microscopic insights for understanding the correlated electronic phases in this class of delafossite metals.

S. Y. and G. L. acknowledge support from the National Key R&D Program of China (Grant No. 2022YFA1402703) and start-up funding from ShanghaiTech University. S. Y. acknowledges support from the National Key R&D Program of China (Grant No. 2020YFA0309602). C. W. acknowledges support from National Natural Science Foundation of China (Grant No. 12004250). Y. Q. acknowledges support from the National Natural Science Foundation of China (Grants No. 52272265, No. U1932217, No. 11974246, and No. 12004252) and the National Key R&D Program of China (Grant No. 2018YFA0704300). G. L. acknowledges Shanghai 2021-Fundamental Research Aera 21JC1404700 for financial support. X. Z. acknowledges the Post-doctoral Special Funds for Theoretical Physics of the National Natural Science Foundation of China (Grant No. 12147124). Part of the calculations were performed at the HPC Platform of ShanghaiTech University Library and Information Services and at the School of Physical Science and Technology.

*These authors contributed equally to this work.

†qiyp@shanghaitech.edu.cn

‡ligang@shanghaitech.edu.cn

§yanshch@shanghaitech.edu.cn

- [1] E. Fradkin, S. A. Kivelson, and J. M. Tranquada, *Rev. Mod. Phys.* **87**, 457 (2015).
- [2] J. C. S. Davis and D.-H. Lee, *Proc. Natl. Acad. Sci. U.S.A.* **110**, 17623 (2013).
- [3] Q. Si, R. Yu, and E. Abrahams, *Nat. Rev. Mater.* **1**, 16017 (2016).
- [4] F. Lechermann and R. Richter, *Phys. Rev. Res.* **2**, 013352 (2020).
- [5] J. A. Sobota *et al.*, *Phys. Rev. B* **88**, 125109 (2013).
- [6] V. Sunko *et al.*, *Sci. Adv.* **6**, eaaz0611 (2020).
- [7] H. Takatsu, S. Yonezawa, C. Michioka, K. Yoshimura, and Y. Maeno, *J. Phys. Conf. Ser.* **200**, 012198 (2010).
- [8] A. P. Mackenzie, *Rep. Prog. Phys.* **80**, 032501 (2017).
- [9] K. P. Ong and D. J. Singh, *Phys. Rev. B* **85**, 134403 (2012).
- [10] R. D. Shannon, D. B. Rogers, and C. T. Prewitt, *Inorg. Chem.* **10**, 713 (1971).
- [11] R. D. Shannon, C. T. Prewitt, and D. B. Rogers, *Inorg. Chem.* **10**, 719 (1971).
- [12] R. D. Shannon, D. B. Rogers, C. T. Prewitt, and J. L. Gillson, *Inorg. Chem.* **10**, 723 (1971).
- [13] H. Takatsu, H. Yoshizawa, S. Yonezawa, and Y. Maeno, *Phys. Rev. B* **79**, 104424 (2009).
- [14] D. Billington *et al.*, *Sci. Rep.* **5**, 12428 (2015).
- [15] H. Takatsu *et al.*, *Phys. Rev. B* **89**, 104408 (2014).
- [16] M. D. Le *et al.*, *Phys. Rev. B* **98**, 024429 (2018).
- [17] H. Takatsu, S. Yonezawa, S. Fujimoto, and Y. Maeno, *Phys. Rev. Lett.* **105**, 137201 (2010).
- [18] H.-J. Noh *et al.*, *Sci. Rep.* **4**, 3680 (2014).
- [19] C. W. Hicks, A. S. Gibbs, L. Zhao, P. Kushwaha, H. Borrmann, A. P. Mackenzie, H. Takatsu, S. Yonezawa, Y. Maeno, and E. A. Yelland, *Phys. Rev. B* **92**, 014425 (2015).
- [20] J. M. Ok, Y. J. Jo, K. Kim, T. Shishidou, E. S. Choi, H.-J. Noh, T. Oguchi, B. I. Min, and J. S. Kim, *Phys. Rev. Lett.* **111**, 176405 (2013).
- [21] F. Lechermann, *Phys. Rev. Mater.* **2**, 085004 (2018).
- [22] F. Lechermann, *npj Comput. Mater.* **7**, 120 (2021).
- [23] H. Takatsu and Y. Maeno, *J. Cryst. Growth* **312**, 3461 (2010).
- [24] G. Pizzi *et al.*, *J. Phys. Condens. Matter* **32**, 165902 (2020).
- [25] A. Georges, G. Kotliar, W. Krauth, and M. J. Rozenberg, *Rev. Mod. Phys.* **68**, 13 (1996).
- [26] G. Kotliar, S. Y. Savrasov, K. Haule, V. S. Oudovenko, O. Parcollet, and C. A. Marianetti, *Rev. Mod. Phys.* **78**, 865 (2006).
- [27] P. Werner, A. Comanac, L. de' Medici, M. Troyer, and A. J. Millis, *Phys. Rev. Lett.* **97**, 076405 (2006).
- [28] See Supplemental Material at <http://link.aps.org/supplemental/10.1103/PhysRevLett.131.116501> for further experimental data and computational details, which includes Ref. [5].
- [29] P. Kong, G. Li, Z. Yang, C. Wen, Y. Qi, C. Felser, and S. Yan, *Nano Lett.* **22**, 5635 (2022).
- [30] F. Mazzola *et al.*, *Proc. Natl. Acad. Sci. U.S.A.* **115**, 12956 (2018).